Energy & Environmental Science

ROYAL SOCIETY OF CHEMISTRY

PAPER

View Article Online
View Journal | View Issue

Cite this: *Energy Environ. Sci.*, 2020, **13**, 622

Interpreting Tafel behavior of consecutive electrochemical reactions through combined thermodynamic and steady state microkinetic approaches†

J. Tyler Mefford, ‡*[ab] Zhenghang Zhao,‡§[c] Michal Bajdich *[c] and William C. Chueh [ab]

Received 23rd August 2019,
Accepted 17th January 2020

DOI: 10.1039/c9ee02697e

rsc.li/ees

Assessing the reaction pathway of multi-electron-transfer reactions is an essential yet difficult task for the rational design of electrocatalysts. In this work, we develop a heuristic approach that combines thermodynamic adsorption energetics calculated through density functional theory with microkinetic modeling using the steady state approximation to interpret the potential-dependent Tafel behavior of consecutive electrochemical reactions. In doing so, we introduce a kinetic framework for *ab initio* calculations that ensures self-consistent adsorption energetics based on kinetically limited adsorbate coverages. The approach is applied to experimental results on $CoO_x(OH)_{2-x}$ single crystal electrocatalyst particles yielding coverage dependent mechanistic information and identification of the rate-limiting step with standard rate constants for the oxygen evolution reaction on the $(11\bar{2}0)$ surfaces of the β-$Co(OH)_2$, β-CoOOH, and CoO_2 bulk phases. This generalizable method enables catalyst benchmarking based on determining the active species involved and associated intrinsic reaction rate constants in consecutive multi-electron-transfer reactions.

Broader context

Electrocatalytic reactions relevant to renewable energy conversion, including the hydrogen evolution reaction, the oxygen reduction and evolution reactions, and the carbon dioxide reduction reaction, involve the net transfer of multiple electrons and ions to yield the desired product. This is accomplished through a stepwise series of consecutive single electron and/or ion transfers with unique chemical intermediates produced at each step. Importantly, the coupling of these intermediates to the electrocatalyst surface determines the efficiency and rate of the overall multi-electron reaction. Additional complexity arises with transition metal oxide electrocatalysts, where the chemical and electronic structure of the oxide is modulated as a function of voltage through the involvement of bulk ion/electron exchange with aqueous electrolytes. In this work, we develop a method to interpret the experimental log current–voltage, or Tafel, relationship of Co (oxy)hydroxide electrocatalysts for the oxygen evolution reaction in alkaline electrolytes. *Ab initio* thermodynamic binding strengths of the intermediates are used to calculate kinetically controlled coverages and reaction barriers through steady-state microkinetic modeling on $CoO_x(OH)_{2-x}$ surfaces with varying bulk proton concentrations (x = 0, 1, 2). This generalizable method has wide applications in deciphering the Tafel behavior and rate-limiting step of consecutive multi-electron transfer reactions.

Introduction

Understanding the fundamental reactions that control the electrolysis of water to oxygen ($2H_2O \rightarrow O_2 + 4H^+ + 4e^-$; oxygen evolution reaction; OER) is a grand challenge in the development of next generation energy conversion technologies.[1,2] First discovered over 200 years ago by Nicholson and Carlisle, a significant amount of effort has been dedicated towards identifying highly active electrocatalysts and understanding material properties that control the OER.[3] Despite these efforts, the identification of an "ideal" catalyst that can operate at the thermodynamic potential (E^0 = 1.23 V *vs.* RHE) still eludes

[a] *Department of Materials Science and Engineering, Stanford University, Stanford, CA 94305, USA. E-mail: tmefford@stanford.edu*
[b] *Stanford Institute for Materials and Energy Sciences, SLAC National Accelerator Laboratory, Menlo Park, CA 94025, USA*
[c] *SUNCAT Center for Interface Science and Catalysis, SLAC National Accelerator Laboratory, Menlo Park, CA 94025, USA. E-mail: bajdich@stanford.edu*

† Electronic supplementary information (ESI) available. See DOI: 10.1039/c9ee02697e

‡ These authors contributed equally to this work.

§ Present address: Department of Chemical and Biomolecular Engineering, University of Notre Dame, Notre Dame, IN 46556, USA.

investigators. Inherent to the difficulties in the search for an ideal catalyst is the underlying complexity of the overall reaction which necessitates four electron transfers, four proton transfers, and the formation of the O–O bond, resulting in a wide array of possible reaction pathways despite a seemingly simplified current–voltage relationship.[4]

Mathematical microkinetic modeling is a powerful tool to interpret how various reaction pathways and rate-determining steps govern the log current density–voltage, or Tafel, relationships. The most common approach uses quasi-equilibrium assumption where reactions that precede the rate-limiting step (RLS) are assumed to proceed rapidly in both forward and reverse directions.[5–7] In addition, only one RLS is assumed to dominate over the entire voltage range of the reaction. Traditionally, solutions to these expressions also assumed certain coverage conditions such that the intermediate involved in the RLS was assumed to approach a coverage of $\theta \approx 0$ or 1 in Langmuir conditions or $\theta \approx 0.2$–0.8 in Temkin conditions.[6,8–13] The result yields a single Tafel slope value that is diagnostic of the reaction mechanism and RLS. Recently, this quasi-equilibrium approach was improved to consider the voltage-dependent coverage of intermediate species preceding and involved in the RLS. The improved approach results in variable Tafel slopes with increasing voltage even for a single RLS.[14] Interestingly, this approach demonstrated that for a given OER reaction mechanism, similar Tafel slope values are predicted amongst differing RLS possibilities. Specifically, all possible RLS reactions yield a limiting Tafel slope of 118 mV dec^{-1} at high overpotential, which although experimentally observed could not be rationalized through previous microkinetic approaches.[10] Thus, only through analyzing the full Tafel data over a wide range in overpotentials and multiple orders of magnitude in current density can the RLS be isolated. However, as will be shown, the quasi-equilibrium approximations oversimplify the kinetic analysis of Tafel slopes which may lead to incorrect determinations about the identity and rate constant of the RLS.

An alternative approach uses the steady state assumption whereby forward and backward rates of each elementary reaction can contribute to the observed overall net rate. Here, no RLS is assumed and multiple reaction steps may be co-rate-limiting over different voltage ranges. Like the quasi-equilibrium approach this method yields voltage-dependent Tafel slopes. Reverse reactions contribute to the observed reaction rate and intermediate coverage where even small changes in the coverage of minority adsorbates will influence the net reaction rates and Tafel slope. Importantly, this approach removes many of the assumptions of the previous quasi-equilibrium approach yielding information that closer approximates the true physics of the reaction. In a number of recent publications, this steady state approach helped differentiate reaction mechanisms of the reverse reaction of the OER, the oxygen reduction reaction (ORR; $O_2 + 4H^+ + 4e^- \rightarrow 2H_2O$), on carbon–metal oxide composite systems.[15–19] Herein, we will demonstrate the utility of the steady state approach in isolating a single RLS that can describe the varying Tafel slope behavior observed on OER electrocatalysts across multiple orders of magnitude in current.

For both the quasi-equilibrium and steady state approaches there remains the issue that the electric field that drives each intermediate reaction, i, of a multi-electron process, the Galvani potential ($\Delta\varphi_i = E - E_i^0$), is unknown. Traditionally, the standard potential for the net reaction is assumed to be the standard potential for each intermediate reaction as well (*i.e.* $E^0 = 1.23$ V *vs.* RHE for the OER).[14] Of course, this assumption is an oversimplification as experimental values for some intermediate reactions have been measured and differ from the overall standard potential (for example the oxidation of the hydroperoxide intermediate at $E^0 = 0.77$ V *vs.* RHE, $HO_2^- + OH^- \rightarrow O_2 + H_2O + 2e^-$).[17] Thus, to calculate standard rate constants, or those that describe the microscopic reversibility of an intermediate reaction at the equilibrium potential, the standard potentials for the intermediate reactions must be measured or calculated.

In order to overcome this limitation, we utilize density functional theory (DFT) calculations, which have become increasingly important to electrocatalyst development and theory.[7,20–30] These methods are based on the calculated thermodynamics of the adsorption strength of proposed intermediates. From these energetics, "potential limiting steps" (PLS) or elementary reactions requiring the largest standard free energy changes are identified. Thus, DFT calculations should yield the standard potentials necessary in describing the Galvani potential. Typically, the kinetic contribution to the reaction barrier is not calculated and the thermodynamic contributions to the barrier are assumed to dominate. Notably, a universal thermodynamic descriptor on oxide surfaces was proposed—the difference in the adsorption strength of an O* intermediate *versus* an OH* intermediate, $\Delta G^0_{O^*} - \Delta G^0_{OH^*}$. Based on the Sabatier principle, an ideal catalyst should have an optimized binding strength for both OH* and O* resulting in a $\Delta G^0_{O^*} - \Delta G^0_{OH^*} = 1.23$ V, equivalent to the standard voltage of the OER. In contrast, no known catalyst can operate at the thermodynamic voltages due to scaling relationships between adsorbate binding strengths which imposes a thermodynamic overpotential of 0.2–0.4 V even for a material with ideal O* adsorption energetics.[31] However, these scaling relationships are based on adsorption energetics for surface coverages defined by thermodynamics rather than kinetics. Only recently, efforts have been made to calculate OER Tafel slopes directly from DFT for well-defined precious metal oxide OER catalysts.[7,32,33] Recent work by Liu *et al.* have investigated the energetics of the RLS transition state as a function of surface electronic charge demonstrating a varying Tafel slope with overpotential.[7,32] Still there remains the issue of defining the surface intermediate coverage during the reaction. In contrast to the thermodynamic predicted coverage generally used in DFT approaches, at any appreciable reaction rate the kinetics of multi-electron transfer reactions impose a concentration overpotential that traps the surface in a coverage dominated by the reactant of the rate-limiting step. Thus, accurate electrocatalyst screening and benchmarking must re-evaluate DFT calculated adsorption energetics through the framework of kinetically limited adsorbate surface coverages.

In this work we develop a combined generalizable thermodynamic and microkinetic modeling approach aimed at resolving three outstanding issues in the interpretation of consecutive multi-electron-transfer electrocatalytic reactions:

(1) The inclusion of forward and backward contributions of all intermediate reaction steps such that reaction pathways where the back reaction is favored (Galvani potential is negative) are accounted for and no *a priori* assumptions are needed in order to calculate the rate-limiting step.

(2) Implicit solutions for the Galvani potential ($\Delta\varphi$) established at the electrode–electrolyte interface for each intermediate step of an overall reaction mechanism such that standard rate constants can be calculated.

(3) The lack of activation barrier calculations in DFT that lead to thermodynamic coverage predictions that do not realistically model experimental conditions.

We apply our improved approach to interpret the electrochemistry of single crystal platelet particles of β-$Co(OH)_2$ in the oxygen evolution reaction.[34–38] Using these particles as model systems, we calculate the thermodynamic adsorption energetics on various $CoO_x(OH)_{2-x}$ bulk phases and corresponding surface facets through DFT. We compare microkinetic models based on the quasi-equilibrium and steady state approaches using the DFT determined potentials of the elementary steps as inputs. The approach reduces the degrees of freedom in modeling variables and a result, we identify the intrinsic rate constants and rate-limiting step on the active $(11\bar{2}0)$ surfaces of the $CoO_x(OH)_{2-x}$ bulk phases for the oxygen evolution reaction.

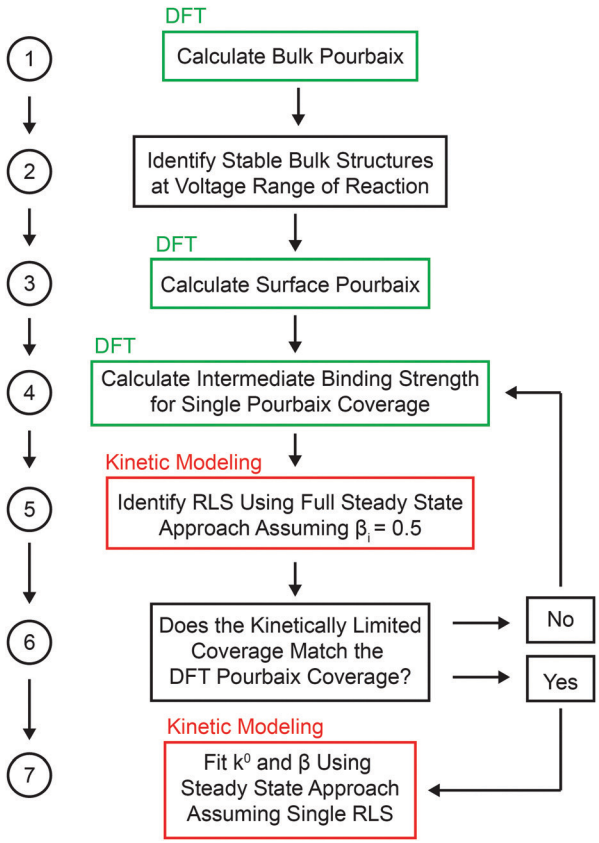

Scheme 1 Flowchart for calculating rate-limiting steps and standard rate constants using combined thermodynamic and microkinetic approaches.

Theoretical approach

Our generalizable, heuristic approach to decipher the Tafel behavior of consecutive electrochemical reactions is shown schematically in Scheme 1. First, in Step 1, an electrocatalytic electrode system of interest is identified, in this case $CoO_x(OH)_{2-x}$, the reaction pathway is specified, and the thermodynamically stable bulk phases are calculated through DFT or measured experimentally. In general, transition metal oxides undergo bulk phase change reactions in aqueous solutions at different applied voltages and these different bulk phases are accounted for and modeled in Step 2.[39] Next, in Step 3, the surface coverage as a function of applied voltage (*i.e.*, surface Pourbaix diagram) is calculated through DFT for a given bulk phase. An iterative process then follows. In Step 4, the binding strength of the reaction intermediates are calculated for a single surface Pourbaix coverage scenario present during the reaction voltage regime, starting from the those present at the standard potential of the OER, 1.23 V *vs.* RHE, and moving anodic in surface Pourbaix coverages in successive iterations until the self-consistency criterion is satisfied. Next, in Step 5, these adsorption energies are input into a microkinetic model where the standard rate constants of each reaction are fit to the current–voltage data using the steady state approach. For completeness, we compare the efficacy of both the quasi-equilibrium and steady state microkinetic modeling approaches in the ESI† which demonstrates the inadequacy of the quasi-equilibrium approach in isolating the identity of the RLS. At this step, the symmetry coefficient (β_i) for each reaction is fixed at the symmetric value of 0.5. The results of the microkinetic modeling allow the self-consistency criterion to be evaluated in Step 6, *i.e.* does the kinetically limited coverage match the coverage used in the DFT calculations of the intermediates adsorption energies? If not, the process is repeated from Step 4 with a new coverage scenario for the DFT calculations until the DFT and kinetically controlled coverages agree. Upon satisfaction of the self-consistency criterion, finally, the RLS is identified and in Step 7 is assumed to dominate over the experimental voltage range. The standard rate constant k^0_{RLS} and β_{RLS} (and $E^0_{Phase\ Change}$ phase-change parameter in the case of a bulk redox-active electrode) are fit to the current–voltage data to yield the intrinsic turnover frequency. In summary, this iterative approach constitutes a rigorous protocol to interpret current–voltage data by sequentially refining DFT energetics and kinetic parameters to ensure self-consistency while minimizing the number of fitting parameters in each successive fitting step.

Results

The bulk DFT-calculated Pourbaix diagram for the Co–H_2O system is presented in Fig. 1a with the bulk phases modeled

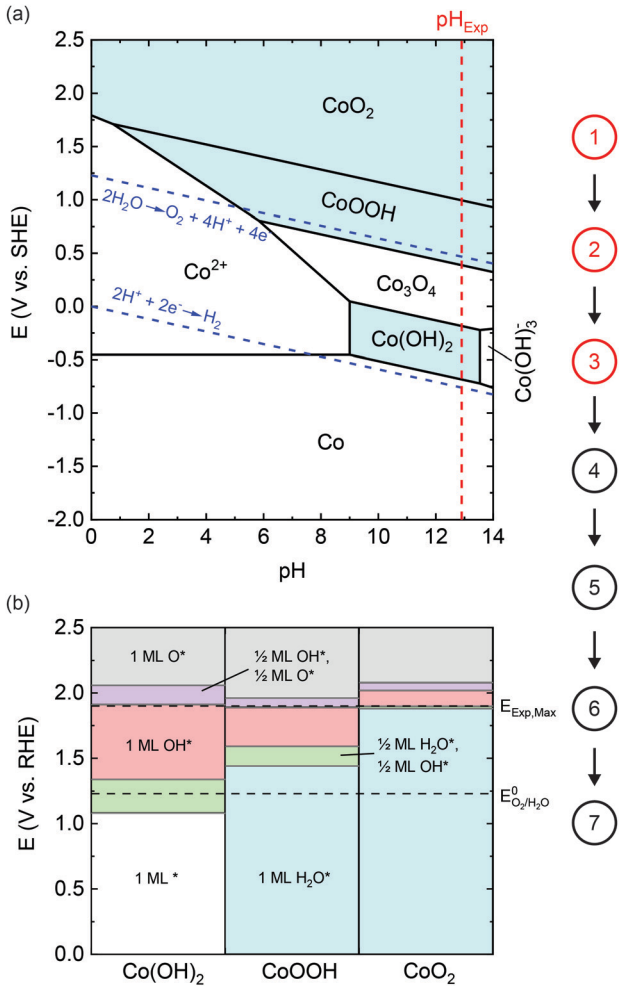

Fig. 1 Bulk and surface Pourbaix Diagram of the $CoO_x(OH)_{2-x}$ system. (a) Bulk Co–H_2O Pourbaix diagram based on experimental formation free energies. The assumed concentration of Co was 10^{-6} mol kg^{-1}.[69] Phases modeled in this study at the experimental pH_{Exp} of 12.9 are shown in the shaded blue region.[34] (b) Potential dependent surface coverages at pH_{Exp} for the $(11\bar{2}0)$ facet of the $CoO_x(OH)_{2-x}$ phases. The different adsorbate coverages are color coded with ML referring to monolayer coverage. The dotted black lines show the standard potential for the OER and the maximum anodic voltage of the experimental data. Surface Pourbaix coverages used in the DFT adsorption energetics calculations fall between these dotted lines.

highlighted in blue (Steps 1 and 2 of our scheme) (see Computational details). We focus on the layered phases in the $CoO_x(OH)_{2-x}$ system including β-$Co(OH)_2$, β-CoOOH, and CoO_2 as these phases share similar structures with only offsets of the CoO_6 layers with respect to each other and 2, 1, or 0 interlayer H atoms, respectively.[39–44] More complicated phases with fractional H stoichiometries will be a subject of our future work.

The surface coverage Pourbaix diagram is calculated as a function of voltage for the $(11\bar{2}0)$ facet of β-$Co(OH)_2$, β-CoOOH, and CoO_2 through density functional theory with the Hubbard-U correction (DFT+*U*) (Step 3 of our scheme). This facet was selected as it was present in the as-synthesized state of the β-$Co(OH)_2$ platelet particles in our previously reported experimental work.[34] These results are shown in Fig. 1b. We focus on adsorbates involved in the elementary reactions of the general adsorbate based OER mechanism used for alkaline electrolytes, where * represents an empty surface site and *i** represents the same surface site covered with the *i* adsorbate:[45]

$$* + OH^- \rightleftharpoons OH^* + e^- \quad (1)$$

$$OH^* + OH^- \rightleftharpoons O^* + H_2O + e^- \quad (2)$$

$$O^* + OH^- \rightleftharpoons OOH^* + e^- \quad (3)$$

$$OOH^* + OH^- \rightleftharpoons * + O_2 + H_2O + e^- \quad (4)$$

For all $(11\bar{2}0)$ surfaces, we have considered at least 6 different surface coverages starting from the clean 1 ML* surface, progressing through 1 ML H_2O^*, $\frac{1}{2}$ ML H_2O^* $\frac{1}{2}$ ML OH*, 1 ML OH*, $\frac{1}{2}$ ML OH* $\frac{1}{2}$ ML O*, and terminating at 1 ML O*. The free energies of these coverages as a function of applied voltage are shown in Fig. S1 (ESI†). Fractional coverages between those mentioned above were also considered for the CoO_2 phase, but they were found to be less stable then the $\frac{1}{2}$ ML or 1 ML coverages. We note that the $(11\bar{2}0)$ surface has 2 adsorption sites per Co atom such that $\frac{1}{2}$ ML H_2O $\frac{1}{2}$ ML OH*, for example, refers to an H_2O molecule and an OH molecule co-adsorbed on the same Co site. From the surfaces considered, the lowest energy coverage at a given potential determines the surface Pourbaix diagram in Fig. 1b. For the β-$Co(OH)_2$ $(11\bar{2}0)$ surface, the calculated coverages with increasing voltage from 0 to 2.5 V *vs.* RHE are 1 ML * (clean surface), $\frac{1}{2}$ ML H_2O^* $\frac{1}{2}$ ML OH* (half OH-covered/half clean surface), 1 ML OH* (fully OH-covered), $\frac{1}{2}$ ML OH* $\frac{1}{2}$ ML O* (half-OH/half-O) and 1 ML O* (fully O-covered) in order to complete the octahedra of the surface Co sites. The β-CoOOH and CoO_2 $(11\bar{2}0)$ exhibited similar surface coverages but were found to prefer having 1 ML of adsorbed water (1 ML H_2O^*) over the clean surface likely due to stabilization from the hydrogen bonding network at the surface. For β-$Co(OH)_2$ it is expected that the higher number of protons in the bulk structure repel excess proton charge of adsorbed water thus preferring unsaturated clean surfaces but that co-adsorbed water helps stabilize the OH* adsorbate.[28,29] The experimental OER voltage range spans 1.4 to 1.9 V *vs.* RHE.[15] Thus for the DFT adsorption energetics and microkinetic calculations we only consider surface Pourbaix coverages from the OER thermodynamic potential, 1.23 V *vs.* RHE, up to the maximum anodic experimental voltage, indicated by the dotted lines in Fig. 1b. For β-$Co(OH)_2$ this includes the $\frac{1}{2}$ ML H_2O^* $\frac{1}{2}$ ML OH* and 1 ML OH* coverages, for β-CoOOH this includes the 1 ML H_2O^*, $\frac{1}{2}$ ML H_2O^* $\frac{1}{2}$ ML OH*, and 1 ML OH* coverages, and for CoO_2 this includes the 1 ML H_2O^* and $\frac{1}{2}$ ML H_2O $\frac{1}{2}$ ML OH* coverages.

Next, the adsorption energetics of reactions (1)–(4), $E^{0'}_{i,DFT}$, are calculated in the DFT thermodynamic approach for a single Co site while all other Co sites have one of the various possible surface Pourbaix coverage conditions mentioned above (Step 4). A schematic of the scenario for the β-$Co(OH)_2$ $(11\bar{2}0)$ facet with 1 ML OH* coverage is shown in Fig. 2. We note that this approach modifies the "true" standard potential of the

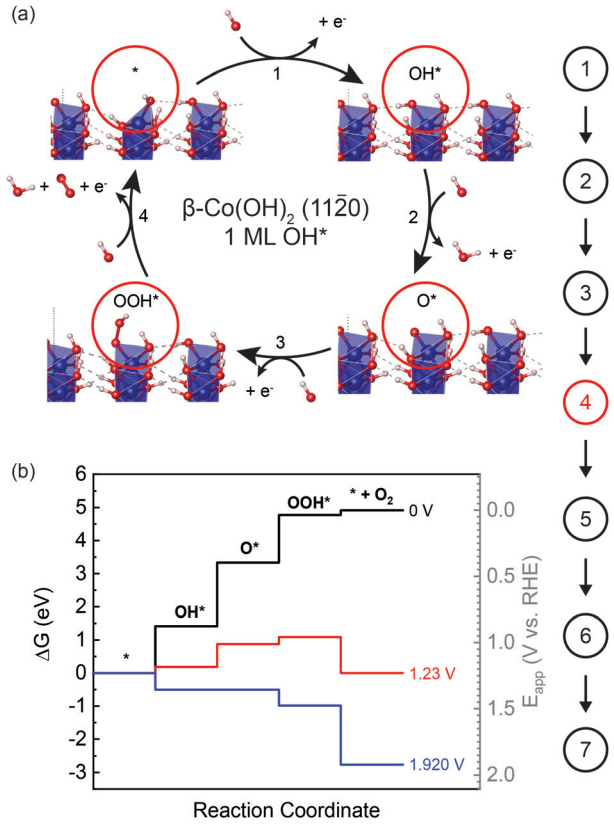

Fig. 2 Example of surface cover condition for calculation of OER adsorbate energetics. (a) OER mechanism on β-$Co(OH)_2$ (11$\bar{2}$0) surface facet with 1 ML OH* DFT coverage condition. The adsorption energy for each intermediate is calculated on a single surface Co site while all other surface Co sites have one of the possible surface Pourbaix coverages at potentials >1.23 V *vs.* RHE. The structures show Co atoms represented as blue spheres, O atoms as red spheres, and H atoms as white spheres. (b) Thermodynamic reaction free energy coordinate calculated for 1 monolayer (ML) of OH* on the β-$Co(OH)_2$ (11$\bar{2}$0) surface. Shown are applied potentials of 0 V (black line), the standard OER potential of 1.23 V (red line), and at the thermodynamic overpotential of 1.920 V where all reaction steps are downhill (blue line).

elementary reaction (*i.e.* the potential for $\frac{1}{2}$ ML coverage of the reactant and $\frac{1}{2}$ ML coverage of the product), E_i^0, through interactions between neighboring adsorbates and the influence of the underlying bulk and surface structures (*i.e.* the potential for each elementary reaction at a single site when all other sites have a particular surface Pourbaix coverage), E_i:[20,35,46]

$$E_{i,\mathrm{DFT}}^{0'} = E_i^0 + \Delta E_i \quad (5)$$

Thus, $E_{i,\mathrm{DFT}}^{0'}$, can be regarded as the kinetic standard potential or the potential for each intermediate reaction on a single site in the presence of a saturated coverage of the reactant adsorbate of the RLS. These results are presented in Table 1 along with the coverage conditions used in the DFT calculations and the potential limiting step (PLS, $\eta_{\mathrm{PLS}} = \max\left[E_{i,\mathrm{DFT}}^{0'} - E_{\mathrm{O_2/H_2O}}^{0}\right]$) shown in bold.

We now introduce a self-consistency criterion for selecting the appropriate $E_{i,\mathrm{DFT}}^{0'}$ values in our analysis. Essentially this criterion evaluates the validity of the ΔE_i term. The self-consistency criterion dictates that the coverage condition used to calculate the individual $E_{i,\mathrm{DFT}}^{0'}$ values is present during the RLS. More specifically, the RLS should lead to a buildup in the surface concentration of the reactant of the RLS (concentration overpotential) such that this reactant dominates the coverage. For example, as shown in Table 1, if the RLS is OH* → O* then the surface should be covered with either $\frac{1}{2}$ ML H_2O* $\frac{1}{2}$ ML OH* or 1 ML of OH* adsorbates (as the $\frac{1}{2}$ ML H_2O $\frac{1}{2}$ ML OH* surface has an OH* adsorbate on each Co site of the (11$\bar{2}$0) surface). We note the traditional thermodynamic approach through DFT calculations follows a similar self-consistency criterion where the potential limiting step (but not necessarily the RLS) is identified and compared to the coverage condition used in the DFT calculations.[20,35,46] However, this approach neglects the concentration overpotential imposed by the kinetics of the elementary reactions. As such, we view a combined thermodynamic and microkinetic approach essential to the evaluation of "true" reaction pathway energetics.

Microkinetic modeling of the oxygen evolution reaction on $CoO_x(OH)_{2-x}$

Next, we use the thermodynamics calculated through DFT as inputs into a microkinetic model to understand the interplay between thermodynamics and kinetics in the observed OER activity of the $CoO_x(OH)_{2-x}$ materials (Step 5 of Scheme 1). We fit the model to our previously reported experimental Brunauer–Emmett–Teller (BET) surface area normalized

Table 1 DFT calculated standard potentials of adsorption based on coverage conditions and $CoO_x(OH)_{2-x}$ phase for the (11$\bar{2}$0) surface facet. The potential limiting step, PLS $\left(\eta_{\mathrm{PLS}} = \max\left[E_{i,\mathrm{DFT}}^{0'} - E_{\mathrm{O_2/H_2O}}^{0}\right]\right)$, is shown in bold. The computational data to reproduce this table is available online *via* catalysis-hub.org[70,71]

Phase	DFT coverage conditions	$E_{1,\mathrm{DFT}}^{0'}$ (V_{RHE}) * ⇌ OH*	$E_{2,\mathrm{DFT}}^{0'}$ (V_{RHE}) OH* ⇌ O*	$E_{3,\mathrm{DFT}}^{0'}$ (V_{RHE}) O* ⇌ OOH*	$E_{4,\mathrm{DFT}}^{0'}$ (V_{RHE}) OOH* ⇌ * + O_2
β-$Co(OH)_2$	$\frac{1}{2}$ ML H_2O* $\frac{1}{2}$ ML OH*	0.063	**2.036**	1.200	1.617
β-$Co(OH)_2$	1 ML OH*	1.414	**1.920**	1.441	0.141
β-CoOOH	1 ML H_2O*	1.123	**1.527**	1.516	0.751
β-CoOOH	$\frac{1}{2}$ ML H_2O* $\frac{1}{2}$ ML OH*	1.131	**2.025**	0.975	0.785
β-CoOOH	1 ML OH*	1.713	**1.836**	1.513	−0.145
CoO_2	1 ML H_2O*	1.041	**2.030**	1.502	0.342
CoO_2	$\frac{1}{2}$ ML H_2O* $\frac{1}{2}$ ML OH*	1.732	**2.118**	0.047	1.019

rotating-disk electrochemistry (RDE) Tafel data, where the BET surface area corresponds to the electrochemically active surface area.[34] Both the quasi-equilibrium and steady state approaches are applied and evaluated on their efficacy in fitting the experimental data. Herein, we present the results of the steady state approach as it more closely approximates the realistic reaction contributions under the Butler–Volmer framework.

The kinetics of the reaction are evaluated through the Butler–Volmer framework:

$$\vec{k}_i = k_i^0 \mathrm{e}^{\left[(1-\beta_i) f\left(E - E_{i,\mathrm{DFT}}^{0'}\right)\right]} \quad (6)$$

$$\overleftarrow{k}_i = k_i^0 \mathrm{e}^{\left[-\beta_i f\left(E - E_{i,\mathrm{DFT}}^{0'}\right)\right]} \quad (7)$$

$$\nu_i = \vec{k}_i \theta_{i,\mathrm{R}} - \overleftarrow{k}_i \theta_{i,\mathrm{P}} \quad (8)$$

where the forward reaction rate $\left(\vec{k}_i\right)$ and backward reaction rate $\left(\overleftarrow{k}_i\right)$ are a function of the intrinsic standard rate constant (k_i^0), symmetry coefficient (β_i), and applied overpotential $\left(E - E_{i,\mathrm{DFT}}^{0'}\right)$ for a given elementary step, and $f = F/RT$ where F is Faraday's constant, R is the ideal gas constant, T is the temperature (298 K), $\theta_{i,\mathrm{R}}$ is the coverage of the reactant adsorbate for reaction i, $\theta_{i,\mathrm{P}}$ is the coverage of the product for reaction i, and ν_i is the net rate of elementary reaction i.

As the RLS on $CoO_x(OH)_{2-x}$ was experimentally found to follow a concerted proton–electron transfer (CPET) step, the elementary reactions are written in a form in which both a proton (hydroxide ion) and an electron are transferred in the same step.[13] For reaction (4), the hydroperoxide anion intermediate (OOH*) is assumed to convert directly to O_2 rather than forming the superoxide O_2* intermediate due to difficulties in modeling the adsorption free energy for the charged superoxide species. Despite this, there is some indication that superoxide may in fact be involved in the OER on Co oxides.[47] In relation to the proposed mechanisms in the literature, notably Cushing and Goodenough's adsorbate mechanism on oxides, and the observations of the superoxide intermediate, a combination of reactions (1) and (4) can be used to interpret the reactivity of the superoxide intermediate through our microkinetic model.[48] The net reaction rates for the elementary reactions are thus:

$$\nu_1 = \vec{k}_1 \theta_* - \overleftarrow{k}_1 \theta_{\mathrm{OH}} \quad (9)$$

$$\nu_2 = \vec{k}_2 \theta_{\mathrm{OH}} - \overleftarrow{k}_2 \theta_{\mathrm{O}} \quad (10)$$

$$\nu_3 = \vec{k}_3 \theta_{\mathrm{O}} - \overleftarrow{k}_3 \theta_{\mathrm{OOH}} \quad (11)$$

$$\nu_4 = \vec{k}_4 \theta_{\mathrm{OOH}} - \overleftarrow{k}_4 \theta_* \quad (12)$$

Note that the activity of the OH^- ion is omitted from the expressions as the RLS was found to follow a CPET pathway such that the overpotential $\left(E - E_{i,\mathrm{DFT}}^{0'}\right)$ is pH independent when evaluated *versus* the reversible hydrogen electrode (RHE). In addition, a_{O_2} is a constant as the experiments were performed in O_2 saturated electrolyte (1 atm) in which the dissolved O_2 defines the standard thermodynamic voltage for the overall 4-electron reaction (E^0 = 1.23 V *vs.* RHE).

The steady state approximation assumes the coverage of a given adsorbate is only voltage dependent such that it is invariant in time:

$$\frac{\mathrm{d}\theta_{\mathrm{OH}}}{\mathrm{d}t} = \nu_1 - \nu_2 = 0 \quad (13)$$

$$\frac{\mathrm{d}\theta_{\mathrm{O}}}{\mathrm{d}t} = \nu_2 - \nu_3 = 0 \quad (14)$$

$$\frac{\mathrm{d}\theta_{\mathrm{OOH}}}{\mathrm{d}t} = \nu_3 - \nu_4 = 0 \quad (15)$$

The total coverage is assumed to approach a monolayer composed of the fractional contribution of non-interacting intermediate species following Langmuir assumptions:

$$\theta_* + \theta_{\mathrm{OH}^*} + \theta_{\mathrm{O}^*} + \theta_{\mathrm{OOH}^*} = 1 \quad (16)$$

The solutions for the adsorbate coverages as a function of voltage for the system of eqn (9)–(16) are included in the ESI.† The current density is thus:

$$j_{\mathrm{model}} = F\Gamma_{\mathrm{geom}}(\nu_1 + \nu_2 + \nu_3 + \nu_4) \quad (17)$$

where Γ_{geom} is the geometric density of Co sites for a given surface facet. The surface facets and geometric site densities are shown in Fig. 3. Importantly, the rate of the RLS determines the total rate such that eqn (17) simplifies to:

$$j_{\mathrm{model}} = 4F\Gamma_{\mathrm{geom}}\nu_{\mathrm{RLS}} \quad (18)$$

The standard rate constants for the elementary reactions are evaluated by fitting eqn (17) to the experimental Tafel behavior of the $CoO_x(OH)_{2-x}$ electrocatalysts through minimization of the RMS log error. Due to the large degrees of freedom in the fitting parameters, $4k_i^0$'s and $4\beta_i$'s, the symmetry coefficient is initially assumed to be 0.5 for all elementary reactions such

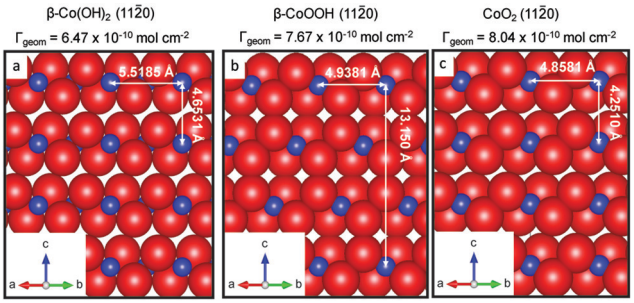

Fig. 3 Active site density of Co atoms in the (11$\bar{2}$0) surface facet $CoO_x(OH)_{2-x}$ phases of the microkinetic model. (a) β-$Co(OH)_2$, (b) β-CoOOH, and (c) CoO_2. Red spheres represent O atoms, blue spheres represent Co atoms.

that there are only the $4k_i^0$ fitting parameters (an assumption we later relax). As shown in the ESI,† the choice of symmetry coefficient does not have a significant influence on the identity of the RLS but also that a symmetric $\beta_i = 0.5$ is associated with a minimum in the RMS log error of the fit. We note that a symmetry coefficient of $\beta_i = 0.5$ is generally predicted by Marcus theory for kinetically controlled electron transfer when the reorganization energy is much larger than the applied overpotential.[7,49–51]

Because all reaction steps are modeled simultaneously, the full electron transfer reaction coordinate can be developed in principle. The barrier height at the standard reaction potential $\left(E_{i,\mathrm{DFT}}^{0'}\right)$ is calculated from the individual rate constants, k_i^0, using the Eyring equation, where κ is the transmission coefficient (assumed to be 1), k_B is Boltzmann's constant, T is the temperature (298 K), h is Planck's constant, and $\Delta G_i^{\ddagger}$ is the Gibbs energy of activation for reaction i:

$$k_i^0 = \frac{\kappa k_B T}{h} e^{\frac{-\Delta G_i^{0,\ddagger}}{RT}} \quad (19)$$

The voltage of the barrier can be calculated through the relation:

$$E_i^{0,\ddagger} = \frac{-\Delta G_i^{0,\ddagger}}{F} \quad (20)$$

And the change in barrier height with applied voltage for the anodic direction can be calculated based on the Butler–Volmer equation as:

$$E_i^{\ddagger} = E_i^{0,\ddagger} - (1-\beta_i)\left(E - E_{i,\mathrm{DFT}}^{0'}\right) \quad (21)$$

The fitting results of the full steady state microkinetic model for the different calculated DFT coverages of the $(11\bar{2}0)$ surface of β-CoOOH are presented in Fig. 4 with their reaction

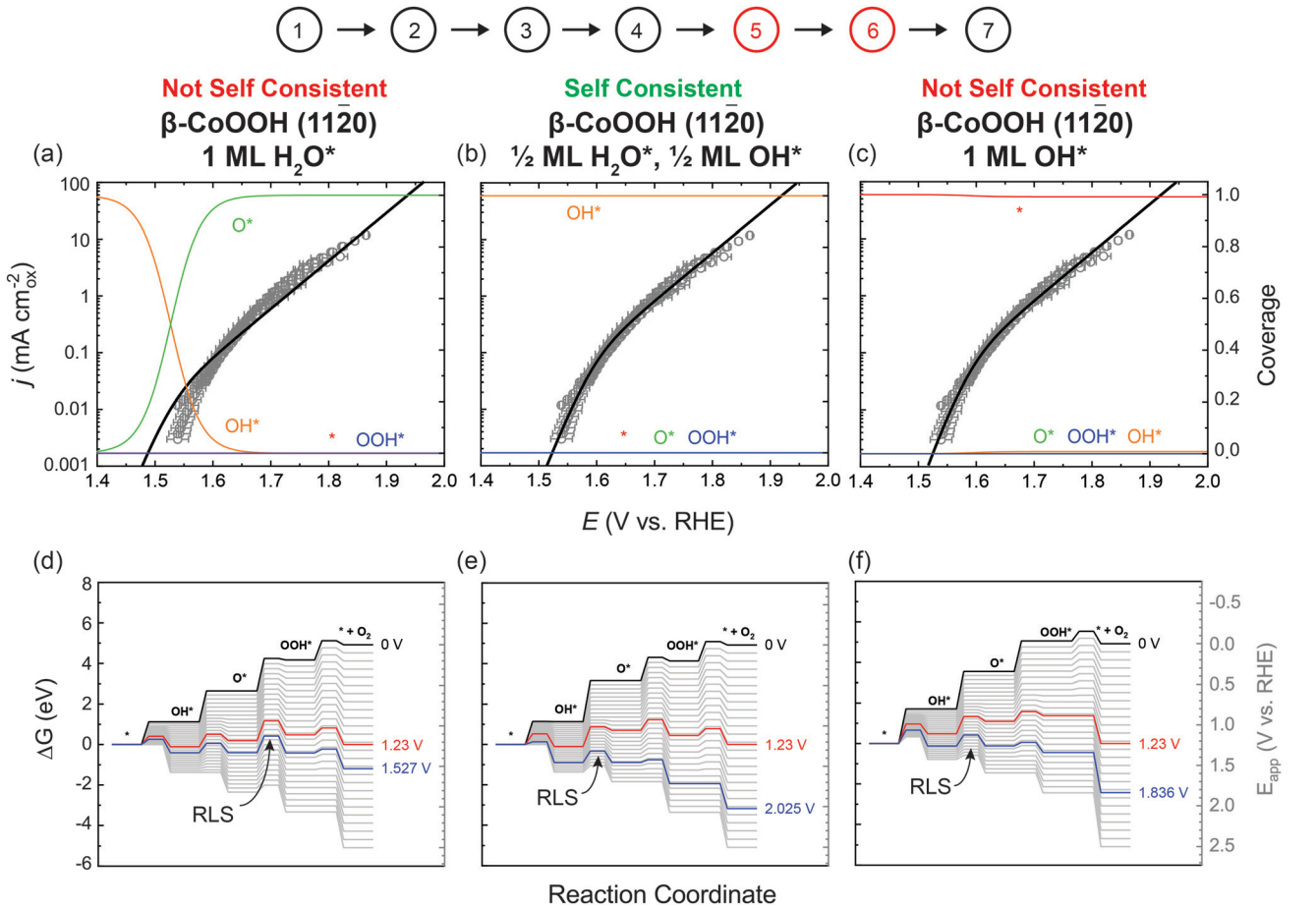

Fig. 4 Steady state microkinetic fits and self-consistency criterion evaluation for the β-CoOOH $(11\bar{2}0)$ surface with different DFT coverages. The fits are shown in black and the coverage predicted by the steady state microkinetic model shown in red for the clean surface, orange for OH*, green for O*, and blue for OOH* for the (a) surface with 1 ML H_2O* DFT coverage, (b) surface with $\frac{1}{2}$ ML H_2O*, $\frac{1}{2}$ ML OH* DFT coverage, and (c) the surface with 1 ML OH* DFT coverage. The full reaction coordinates at applied voltages from 0 to 2.5 V *vs.* RHE in 0.1 V increments are shown for the (d) surface with 1 ML H_2O* DFT coverage, (e) surface with $\frac{1}{2}$ ML H_2O*, $\frac{1}{2}$ ML OH* DFT coverage, and (f) the surface with 1 ML OH* DFT coverage. The reaction coordinates at the standard OER potential (E^0 = 1.23 V *vs.* RHE) and the PLS for the given bulk phase and surface are shown in red and blue, respectively. The RLS is highlighted and compared to the DFT coverage to calculate the thermodynamic adsorbate energetics. Only the β-CoOOH $(11\bar{2}0)$ surface with $\frac{1}{2}$ ML H_2O*, $\frac{1}{2}$ ML OH* DFT coverage fits the self-consistency criterion where the kinetics traps the surface in a dominant OH* coverage due to a RLS of OH* → O*.

coordinates at the thermodynamic OER potential (1.23 V) and at the potential of the DFT potential limiting step plotted as red and blue lines, respectively. With the RLS's identified, we can now evaluate the self-consistency criterion (Step 6). In Fig. 4, there are three coverage scenarios for the β-CoOOH $(11\bar{2}0)$ surface, 1 ML H_2O^*, $\frac{1}{2}$ ML H_2O^* $\frac{1}{2}$ ML OH*, and 1 ML OH*, which are associated with RLS's of O* → OOH*, OH* → O*, and * → OH*, respectively. For these coverage conditions and RLS's, only one scenario is self-consistent: the $\frac{1}{2}$ ML H_2O $\frac{1}{2}$ ML OH* case (RLS: OH* → O*) where the kinetics imposes a concentration overpotential and traps the surface in the same coverage condition used to calculate the adsorption energetics through DFT. Thus, we discard the other scenarios as non-physical. The standard rate constants for the DFT self-consistent coverages for the $(11\bar{2}0)$ surface of the $CoO_x(OH)_{2-x}$ bulk phases with their 95% confidence intervals and RMS log error are presented in Table 2 with the identified RLS bolded. In the reaction coordinates, the change in free energies of the reactions and barrier heights are shown from an applied voltage of 0 to 2.5 V *vs.* RHE in 0.1 V steps. A description of the 95% confidence interval calculations is included in the ESI.† Fits for the DFT-self-consistent coverage conditions for other $CoO_x(OH)_{2-x}$ bulk phases are shown in Fig. S6 (ESI†) and results for non-self-consistent phases are presented in Fig. S7 and Table S6 in the ESI.†

While the full steady state approach results in excellent fits of the observed experimental Tafel data for all phases considered, examination of the 95% confidence intervals in Table 2 shows a high variance for the standard reaction rates that are not the RLS. This suggests that a single RLS may be dominant over the whole experimental voltage range. Indeed, although the steady state modeling yields excellent fits, the steady state approximation in its full form likely suffers from over parameterization which leads to these large covariances between rate constants of non-RLS reactions. One interpretation of the high covariance between the standard rate constants is the DFT predicted standard potentials have some error as no solvent was implicitly included in the model which has been shown to shift the calculated energetics of oxygen reduction by up to 0.5 eV on Pt surfaces and less on oxide surfaces.[52,53] However, the solvation error should only affect the adsorption of hydroxide * → OH* while other steps are only weakly affected by the solvation energy.[53] More likely, however, is the active phase for the OER is potential dependent.[6,7] From our previous work, we found that if the scan rates were increased to above 150 mV s^{-1} a second redox peak incipient with the OER could be separated suggesting evolution of the bulk phase concomitant with the OER. This suggests that the OER is dependent not only on the thermodynamics of adsorbate coverage, but also on the thermodynamics of the bulk/surface structural conversion reactions.

We consider a bulk redox transformation in the microkinetic model by adding a reaction that describes the fraction of the active phase at the surface of the electrocatalyst particles. Specifically, rather than modeling a phase transformation explicitly, we use a solid solution approximation, a schematic of which is shown in Fig. 5. This reaction is assumed to be in equilibrium and only controls the active site fraction at the surface (denoted by brackets) but is not considered an additional kinetic step in the OER:

$$E = E^0_{\text{Phase Change}} + \frac{RT}{F}\ln\frac{[\text{Oxidized } CoO_x(OH)_{2-x} \text{ Species}]}{[\text{Reduced } CoO_x(OH)_{2-x} \text{ Species}]} \quad (22)$$

The same three thermodynamically predicted bulk phases modeled by the DFT analysis are considered. This means that as the potential is increased β-$Co(OH)_2$ converts to β-CoOOH or β-CoOOH coverts to CoO_2 at the potential of $E^0_{\text{Phase Change}}$, where $E^0_{\text{Phase Change}}$ is now included as an additional fitting parameter:

$$\beta\text{-}Co(OH)_2 + OH^- \rightarrow \beta\text{-CoOOH} + H_2O + e^- \quad (23)$$

$$\beta\text{-CoOOH} + OH^- \rightarrow CoO_2 + H_2O + e^- \quad (24)$$

Given the limited voltage range of the experimental OER data, only a single "phase change" reaction is considered with only one end member considered to be the active phase (in the modeling the end member considered active is labeled). Thus as the potential is increased, if β-$Co(OH)_2$ is the active phase it

Table 2 Steady state microkinetic modeling standard rate constants, k_i^0, with 95% confidence intervals and RMS log error for the fit on the DFT self-consistent $CoO_x(OH)_{2-x}$ $(11\bar{2}0)$ surfaces. The rate-limiting step is bolded

Phase	DFT coverage conditions	Reaction step	k_i^0 (s^{-1})	$E^{0'}_{i,\text{DFT}}$ (V_{RHE})	RMS log error
β-$Co(OH)_2$	1 ML OH*	* → OH*	$6 \times 10^3 \pm 2 \times 10^7$	1.414	1.16
		OH* → O*	**239 ± 8**	**1.920**	
		O* → OOH*	$(7.6 \pm 0.6) \times 10^3$	1.441	
		OOH* → * + O_2	$2 \times 10^3 \pm 1 \times 10^7$	0.141	
β-CoOOH	$\frac{1}{2}$ ML H_2O^*	* → OH*	$1 \times 10^3 \pm 2 \times 10^9$	1.131	1.16
	$\frac{1}{2}$ ML OH*	**OH* → O***	$\mathbf{(1.56 \pm 0.1) \times 10^3}$	**2.025**	
		O* → OOH*	43 ± 3	0.975	
		OOH* → * + O_2	$2 \times 10^3 \pm 3 \times 10^9$	0.785	
CoO_2	$\frac{1}{2}$ ML H_2O^*	* → **OH***	**5.0 ± 0.2**	**1.732**	1.16
	$\frac{1}{2}$ ML OH*	OH* → O*	$(2.1 \pm 0.2) \times 10^6$	2.118	
		O* → OOH*	$1 \times 10^7 \pm 2 \times 10^{13}$	0.047	
		OOH* → * + O_2	$6 \times 10^3 \pm 1 \times 10^{10}$	1.019	

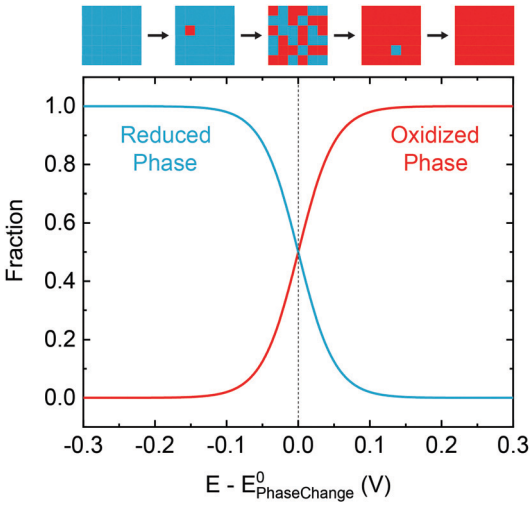

Fig. 5 Fraction of reduced and oxidized $CoO_x(OH)_{2-x}$ species *versus* voltage. The distribution of the bulk phase is assumed to follow the ideal solution model such that there is no interaction between different phases at the surface of the crystal.

is expected to decrease in fraction, whereas if β-CoOOH or CoO_2 is the active phase they are expected to increase in fraction.

The current density can now be expressed as:

$$j = 4F\Gamma_{geo}[\text{Active } CoO_x(OH)_{2-x} \text{ Species}]\nu_{RLS} \quad (25)$$

Considering that a single RLS dominates over the experimental voltage range, we further reduce the degrees of freedom by only fitting the value of the standard rate constant of the RLS and setting all other rate constants to $k^0_{i\neq RLS} = 6.21 \times 10^{12}\ s^{-1}$, corresponding to a voltage barrier of $E^{0,\ddagger}_{i\neq RLS} = 0$ based on eqn (19) and (20). In addition, rather than assuming the symmetry coefficient of the RLS was $\beta_{RLS} = 0.5$, we now fit β_{RLS} as well and include the contribution of a bulk phase change reaction through fitting $E^0_{\text{Phase Change}}$ (Step 7).

The results for the DFT-microkinetic self-consistent scenarios are presented in Fig. 6a–c and the values of k^0_{RLS}, β_{RLS}, and $E^0_{\text{Phase Change}}$ with their 95% confidence intervals and RMS log error are presented in Table 3. We note that insufficient knowledge in the relationship between BET surface area and electrochemically active surface area to appropriately normalize the experimental current density may scale the standard rate constant of the RLS, k^0_{RLS}, but does not change its identity. While the inclusion of $E^0_{\text{Phase Change}}$ improves the fit for the β-$Co(OH)_2$ case, the current density decreases rapidly at high overpotential which was not observed experimentally. We believe this final approach is the closest approximation to the "true" physics of the system and thus can discard the β-$Co(OH)_2$ $(11\bar{2}0)$ surface as an active surface for the OER. Indeed, at open-circuit conditions where β-$Co(OH)_2$ is assumed to be the bulk phase there is no spontaneous evolution of oxygen. For the $(11\bar{2}0)$ surfaces of β-CoOOH and CoO_2 the fits are significantly improved by the addition of $E^0_{\text{Phase Change}}$ as are the variances of the three fitting parameters in comparison to the full steady state approach. As a comparison, results using the single RLS assumption for the steady state approach without a bulk phase change reaction are presented in the ESI,† Fig. S8 and Table S7. The fitting results of the single RLS steady state model with and without the phase-change reaction for the other considered surfaces and coverage conditions are included in Fig. S9 and Tables S8 and S9 in the ESI.† With this

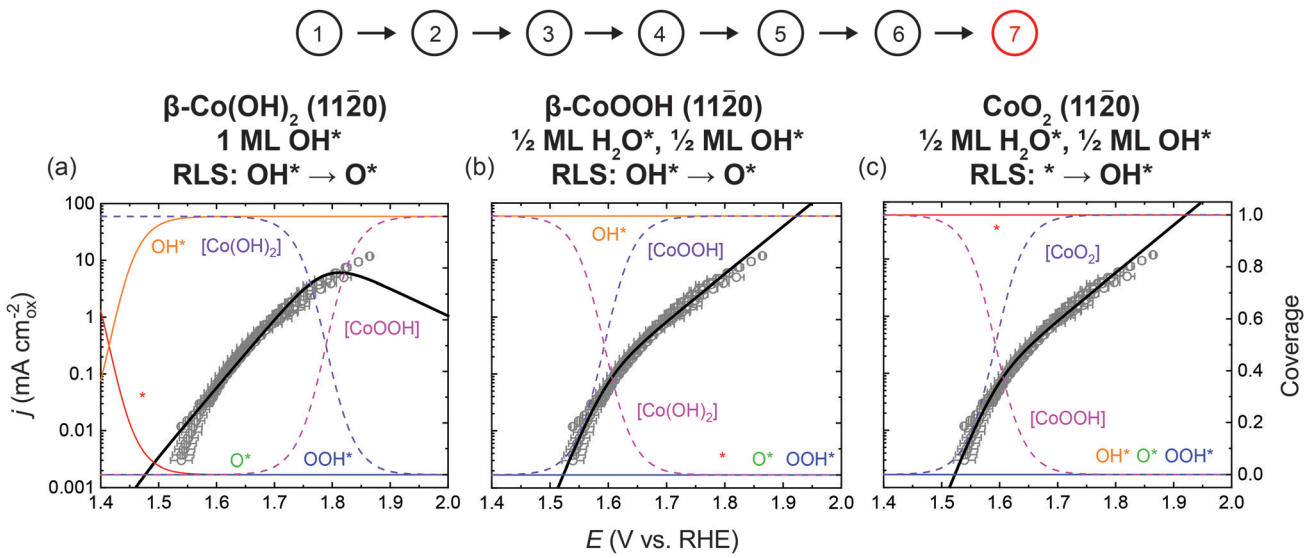

Fig. 6 Steady state microkinetic fits for the DFT self-consistent $CoO_x(OH)_{2-x}$ $(11\bar{2}0)$ surfaces assuming a single RLS dominates and contributions from bulk phase-change reactions. (a–c) Show the single RLS steady state fit including the contribution of a bulk phase change reaction. The fits are shown in black and the coverage predicted by the steady state microkinetic model shown in red for the clean surface, orange for OH*, green for O*, and blue for OOH*, purple for the active phase, and magenta for the inactive phase for the DFT self-consistent scenarios on the (a) β-$Co(OH)_2$ $(11\bar{2}0)$ surface with 1 ML OH* coverage, (b) the β-CoOOH $(11\bar{2}0)$ surface with $\frac{1}{2}$ ML H_2O*, $\frac{1}{2}$ ML OH* coverage, and (c) the CoO_2 $(11\bar{2}0)$ surface with $\frac{1}{2}$ ML H_2O*, $\frac{1}{2}$ ML OH* coverage. We note that the calculated adsorbate coverages correspond to the coverage only on the active phase.

Table 3 Steady state microkinetic modeling standard rate constants, k_i^0, symmetry coefficients, β_i, and phase change voltages, $E^0_{\text{Phase Change}}$, with 95% confidence intervals and RMS log error for fits assuming a single RLS dominates the reaction kinetics and that the concentration of surface phase is voltage dependent on the DFT self-consistent $CoO_x(OH)_{2-x}$ ($11\bar{2}0$) surfaces. These scenarios are considered to adopt the single phase noted in the table

Phase	DFT coverage conditions	RLS	k^0_{RLS} (s^{-1})	β_{RLS}	$E^0_{\text{Phase Change}}$ (V_{RHE})	RMS log error
β-$Co(OH)_2$	1 ML OH*	OH* → O*	1677.51 ± 0.05	0.283 ± 0.001	1.790 ± 0.003	1.81
β-CoOOH	$\frac{1}{2}$ ML H_2O* $\frac{1}{2}$ ML OH*	OH* → O*	1700 ± 40	0.507 ± 0.003	1.593 ± 0.003	1.16
CoO_2	$\frac{1}{2}$ ML H_2O* $\frac{1}{2}$ ML OH*	* → OH*	4.98 ± 0.09	0.51 ± 0.01	1.593 ± 0.003	1.16

approach, the RLS on the ($11\bar{2}0$) surface of β-CoOOH with $\frac{1}{2}$ ML H_2O* $\frac{1}{2}$ ML OH* is identified as OH* → O* with a standard rate constants of 1677 s^{-1} (1.3×10^{-6} mol cm^{-2} s^{-1}) and the RLS of the ($11\bar{2}0$) surfaces of CoO_2 with $\frac{1}{2}$ ML H_2O* $\frac{1}{2}$ ML OH* is identified as * → OH* with a standard rate constant of 5.0 s^{-1} (4.0×10^{-9} mol cm^{-2} s^{-1}), respectively. These results agree well with reports by Bergmann *et al.* on the presence of four and five fold coordinated cobalt ions during the OER suggestive of empty terminal surface sites on the ($11\bar{2}0$) surface.[54,55] $E^0_{\text{Phase Change}}$ takes values of 1.593 V *vs.* RHE for the ($11\bar{2}0$) surfaces of both β-CoOOH and CoO_2. Analysis of the bulk Pourbaix diagram (Fig. 1a) suggests that the conversion of $Co(OH)_2$ → CoOOH should occur at lower potentials, E^0 = 1.150 V *vs.* RHE, and the CoOOH → CoO_2 conversion should occur at higher potentials, E^0 = 1.758 V *vs.* RHE, which makes identification of the correct active bulk/surface phase difficult.[34,35] In regards to this, there is a significant amount of discrepancy in the literature as to the presence of Co^{IV} ions during the OER. While certain studies on electrodeposited amorphous CoO_x films suggest the presence of up to 10–25% Co^{IV} during the OER as measured through *ex situ* electron paramagnetic resonance (EPR) or through *in situ* Extended X-ray Absorption Fine Structure (EXAFS), other *operando* studies have only verified the existence of CoOOH and to date no crystalline CoO_2 has been observed in aqueous solutions.[42,56–58] While the value for CoO_2 is closer to the bulk Pourbaix predicted value, it still ∼150 mV negative of the predicted potential. However the fit $E^0_{\text{Phase Change}}$ value is very close to the experimentally observed redox peak for the $CoO_x(OH)_{2-x}$ particles which was observed at $E \approx 1.55$ V *vs.* RHE.[34] Because the fit results are adequate for both β-CoOOH and CoO_2 scenarios, the development of *operando* experiments capable of distinguishing between these phases is needed to isolate the correct physical model of OER on the $CoO_x(OH)_{2-x}$ system.

For further insights into the results of the microkinetic and thermodynamic modeling, we examine the Bader charges, q, of the Co active site and O containing adsorbate and the local magnetic moments, m, of the Co active site for the different surfaces through DFT. We note that the Bader charge is a qualitative description of the oxidation state as seen in the scatter of the values and due to the covalent nature of the metal–ligand bonding. Still, comparing the Bader charge evolution for Co and O in different reaction steps can help interpret the chemical rationale behind the kinetic barrier of the RLS. Although we do not assign oxidation states for Co in this work, previous work has suggested a Bader charge of q: Co ≈ 1.35, 1.45, and >1.55 for Co^{2+}, Co^{3+}, and Co^{4+}, respectively.[35] The results for the DFT self-consistent surfaces are presented in Table 4 with the reactant and product adsorbates involved in the RLS bolded (DFT non-self-consistent surfaces are presented in ESI,† Table S10). Looking at the relative Bader charge changes of the RLS on the ($11\bar{2}0$) β-CoOOH $\frac{1}{2}$ ML H_2O* $\frac{1}{2}$ ML OH* surface, the oxidation state of the Co active site atom does not change while the charge of oxygen radical adsorbate does. This implies a change in the localization of the electron hole from the Co atom to the adsorbed O* radical which is in contrast to the acid–base mechanism proposed by Cushing and Goodenough in which transition metal active sites with a bound protonated adsorbate oxygen radical assume a lower oxidation state, n+, and transition metal active sites with a bound unprotonated adsorbate radical assume an higher oxidation state, $(n + 1)$+.[48,59] This implies that the kinetic barrier in these reactions is the formation of the higher oxide where the generation of a localized electron hole on the O* adsorbate is preferred over a localized electron hole on the transition metal active site.[25,60] We note that highly covalent Co oxide systems, such as the perovskite $SrCoO_{3-\delta}$, have been shown to lower the OER kinetic barrier of this oxygen hole generation through charge transfer between lattice O and Co atoms in the surface of the crystal to yield much more active catalysts.[61] Thus insights gained from this combined approach can serve as activity descriptors to rationally design increased activity in electrocatalytic systems.

Table 4 Bader charges q (in units of electrons) of Co active site and O-containing adsorbate and magnetic moment m (in units of μ_B) for Co active site on the different DFT self-consistent ($11\bar{2}0$) surfaces of $CoO_x(OH)_{2-x}$. Adsorbates involved in RLS are bolded. Note that q: O is the total charge of the O adsorbate (both O atoms for OOH*)

Phase	DFT coverage conditions	Adsorbate	q: Co	q: O	$\lvert m\rvert$
$Co(OH)_2$	1 ML OH*	*	1.38	—	1.90
		OH*	**1.47**	**−1.07**	**1.04**
		O*	**1.47**	**−0.46**	**1.14**
		OOH*	1.45	−1.03	1.07
CoOOH	$\frac{1}{2}$ ML H_2O*	*	1.46	—	2.15
	$\frac{1}{2}$ ML OH*	**OH***	**1.45**	**−1.02**	**0.86**
		O*	**1.46**	**−0.44**	**1.07**
		OOH*	1.41	−0.83	0.99
CoO_2	$\frac{1}{2}$ ML H_2O*	*	**1.41**	—	**1.13**
	$\frac{1}{2}$ ML OH*	**OH***	**1.46**	**−0.99**	**1.11**
		O*	1.46	−0.39	1.18
		OOH*	1.42	−0.72	1.06

Conclusion

The results presented herein describe a combined thermodynamic and microkinetic approach to interpret Tafel behavior of consecutive electrochemical reactions and isolate the nature of the mechanism and rate-limiting step. This approach was applied to experimental data on the single crystal $CoO_x(OH)_{2-x}$ system by considering all possible potential dependent bulk and surfaces phases that may develop during the OER. Of the $(11\bar{2}0)$ surfaces of the $CoO_x(OH)_{2-x}$ phases, β-$Co(OH)_2$ was found to be inactive for the OER while β-CoOOH and CoO_2 were found to be potentially active phases for the OER. On these surfaces, the rate-limiting and potential-limiting step of OH* → O* were found to agree for the β-CoOOH surface with an intrinsic standard rate constant of $\sim$1700 s^{-1}. On the CoO_2 surface the potential limiting step was found to be OH* → O* while the rate-limiting step was determined to be * → OH* with an intrinsic standard rate constant of $\sim$5 s^{-1}. Thus, the results demonstrate the importance of integrating a kinetic framework into the use of DFT calculations for electrocatalysis. Differentiating between these phases to isolate the true species responsible for the OER requires the development of spatially resolved and surface sensitive *operando* techniques and will be the subject of future work.

This work provides a framework for evaluating the Tafel behavior of consecutive electrochemical reactions using both thermodynamic and kinetic theory which may be applied generally to electrocatalytic reactions to evaluate mechanistic reaction pathways. Importantly, we introduce the kinetic self-consistency criterion which constrains the DFT approach to calculate adsorption energies on kinetically controlled surface coverages. We note that this should only be viewed as heuristic approach given current limitations in calculating the full reaction pathways for consecutive reactions. As computational methods advance, the reaction barriers may be calculated through molecular dynamics approaches and then fed into the full-steady state model where the iterative scheme would still operate until the predicted thermodynamics and kinetics yield ideal fits for the experimental data.[32,62–64]

Methods

Computational details

First-principle calculations were performed within the framework of density functional theory (DFT) as implemented in the plane-wave set Vienna ab initio Simulation Package (VASP) code. The plane-wave potentials from the VASP PAW library were employed (PAW_PBE Co 02Aug2007, PAW_PBE O 08Apr2002, and PAW_PBE H 15Jun2001). The optimized bulk structures were adopted from ICSD database for β-$Co(OH)_2$, β-CoOOH and CoO_2.[43,65,66] The bulks were fully relaxed under 500 eV energy cut-off for plane-wave basis-set, and *k*-point sampling of 4 × 4 × 3 for α phases and 4 × 4 × 1 for β phase. PBE functional with Hubbard-U correction of 3.32 eV to d-electrons of Co atoms were used during the calculations.[67,68]

All surfaces were modeled with the same 500 eV energy cut-off as two-dimensional periodic structures with be 15 Å vacuum on the $(11\bar{2}0)$ surface direction to avoid interaction between adjacent surfaces and dipole correction was turned on for the vacuum direction. There were 3 × 2 × 3 CoO_6 octahedra along each direction, and the bottom three layers of Co were fixed. The *k*-point sampling of the Brillouin zone was obtained using a 2 × 4 × 1 grid generating meshes with their origin centered at the gamma (Γ) point. The *k*-point mesh and energy cut off were chosen to ensure that the energies were converged within 1 meV per atom. All calculations were spin-polarized and were completed until the force of the system converges to 0.02 eV $Å^{-1}$. Zero-point energies and entropies were determined by vibrational frequencies under the temperature of 298 K to calculate free energies of adsorption. The surface Pourbaix diagrams were constructed from free energies of all coverages are calculated with respect to gas phase H_2O and H_2. Adsorption energies (ΔE) are included in the ESI† (Table S11) and vibrational and free-energy corrections to convert ΔE to ΔG are included in Table S12 (ESI†).

Microkinetic modeling

The systems of algebraic equations were first solved using Mathematica 10.3 (Wolfram Research) software. The models were fit to the previously published Tafel data on the single crystal β-$Co(OH)_2$ electrocatalysts and the 95% confidence intervals were calculated using the MATLAB R2018b (MathWorks) software.

Conflicts of interest

There are no conflicts to declare.

Acknowledgements

J. T. M. and W. C. C. gratefully acknowledge financial support through the Department of Energy, Office of Basic Energy Sciences, Division of Materials Sciences and Engineering under contract no. DE-AC02-76SF00515. Z. Z. and M. B. acknowledge financial support by the U.S. Department of Energy, Office of Science, Office of Basic Energy Science, *via* Grant DE-SC0008685 to the SUNCAT Center of Interface Science and Catalysis. The authors would like to acknowledge the use of the computer time allocation for the ''Transition metal-oxide and metal surfaces: applications and reactivity trends in catalysis'' at the National Energy Research Scientific Computing Center, a DOE Office of Science User Facility supported by the Office of Science of the U.S. Department of Energy under Contract No. DE-AC02-05CH11231.

References

1 H. Dau, C. Limberg, T. Reier, M. Risch, S. Roggan and P. Strasser, *ChemCatChem*, 2010, **2**, 724–761.

2 N.-T. Suen, S.-F. Hung, Q. Quan, N. Zhang, Y.-J. Xu and H. M. Chen, *Chem. Soc. Rev.*, 2017, **46**, 337–365.
3 W. Nicholson, *A Journal of Natural Philosophy, Chemistry and the Arts*, G. G. and J. Robinson, 1797.
4 M. T. M. Koper, *J. Electroanal. Chem.*, 2011, **660**, 254–260.
5 J. O. Bockris, A. K. N. Reddy and M. E. Gamboa-Aldeco, *Modern Electrochemistry 2A: Fundamentals of Electrodics*, Springer, USA, 2nd edn, 2000.
6 A. Holewinski and S. Linic, *J. Electrochem. Soc.*, 2012, **159**, H864–H870.
7 Y.-H. Fang and Z.-P. Liu, *ACS Catal.*, 2014, **4**, 4364–4376.
8 J. O. Bockris, *J. Chem. Phys.*, 1956, **24**, 817–827.
9 B. E. Conway and B. V. Tilak, in *Advances in Catalysis*, ed. D. D. Eley, H. Pines and P. B. Weisz, Academic Press, 1992, vol. 38, pp. 1–147.
10 A. Damjanovic, A. Dey and J. O. Bockris, *Electrochim. Acta*, 1966, **11**, 791–814.
11 J. O. Bockris and T. Otagawa, *J. Phys. Chem.*, 1983, **87**, 2960–2971.
12 J. O. Bockris and T. Otagawa, *J. Electrochem. Soc.*, 1984, **131**, 290–302.
13 Y. Surendranath, M. W. Kanan and D. G. Nocera, *J. Am. Chem. Soc.*, 2010, **132**, 16501–16509.
14 T. Shinagawa, A. T. Garcia-Esparza and K. Takanabe, *Sci. Rep.*, 2015, **5**, 13801.
15 J. Tyler Mefford, A. A. Kurilovich, J. Saunders, W. G. Hardin, A. M. Abakumov, R. P. Forslund, A. Bonnefont, S. Dai, K. P. Johnston and K. J. Stevenson, *Phys. Chem. Chem. Phys.*, 2019, **21**, 3327–3338.
16 T. Poux, A. Bonnefont, G. Kéranguéven, G. A. Tsirlina and E. R. Savinova, *ChemPhysChem*, 2014, **15**, 2108–2120.
17 T. Poux, A. Bonnefont, A. Ryabova, G. Kéranguéven, G. A. Tsirlina and E. R. Savinova, *Phys. Chem. Chem. Phys.*, 2014, **16**, 13595–13600.
18 A. S. Ryabova, A. Bonnefont, P. Zagrebin, T. Poux, R. Paria Sena, J. Hadermann, A. M. Abakumov, G. Kéranguéven, S. Y. Istomin, E. V. Antipov, G. A. Tsirlina and E. R. Savinova, *ChemElectroChem*, 2016, **3**, 1667–1677.
19 A. S. Ryabova, A. Bonnefont, P. A. Simonov, T. Dintzer, C. Ulhaq-Bouillet, Y. G. Bogdanova, G. A. Tsirlina and E. R. Savinova, *Electrochim. Acta*, 2017, **246**, 643–653.
20 I. C. Man, H.-Y. Su, F. Calle-Vallejo, H. A. Hansen, J. I. Martínez, N. G. Inoglu, J. Kitchin, T. F. Jaramillo, J. K. Nørskov and J. Rossmeis, *ChemCatChem*, 2011, **3**, 1159–1165.
21 J. K. Nørskov, J. Rossmeisl, A. Logadottir, L. Lindqvist, J. R. Kitchin, T. Bligaard and H. Jónsson, *J. Phys. Chem. B*, 2004, **108**, 17886–17892.
22 S. a Akhade and J. R. Kitchin, *J. Chem. Phys.*, 2012, **137**, 084703.
23 A. Vojvodic, F. Calle-Vallejo, W. Guo, S. Wang, A. Toftelund, F. Studt, J. I. Martínez, J. Shen, I. C. Man, J. Rossmeisl, T. Bligaard, J. K. Nørskov and F. Abild-Pedersen, *J. Chem. Phys.*, 2011, **134**, 244509.
24 F. Calle-Vallejo, N. G. Inoglu, H.-Y. Su, J. I. Martínez, I. C. Man, M. T. M. Koper, J. R. Kitchin and J. Rossmeisl, *Chem. Sci.*, 2013, **4**, 1245–1249.
25 F. Calle-Vallejo, O. A. Diaz-Morales, M. J. Kolb and M. T. M. Koper, *ACS Catal.*, 2015, **5**, 869–873.
26 J. K. Nørskov, T. Bligaard, J. Rossmeisl and C. H. Christensen, *Nat. Chem.*, 2009, **1**, 37–46.
27 E. M. Fernández, P. G. Moses, A. Toftelund, H. A. Hansen, J. I. Martínez, F. Abild-Pedersen, J. Kleis, B. Hinnemann, J. Rossmeisl, T. Bligaard and J. K. Nørskov, *Angew. Chem., Int. Ed.*, 2008, **47**, 4683–4686.
28 F. Abild-Pedersen, J. Greeley, F. Studt, J. Rossmeisl, T. R. Munter, P. G. Moses, E. Skúlason, T. Bligaard and J. K. Nørskov, *Phys. Rev. Lett.*, 2007, **99**, 016105.
29 A. Kakekhani, L. T. Roling, A. Kulkarni, A. A. Latimer, H. Abroshan, J. Schumann, H. AlJama, S. Siahrostami, S. Ismail-Beigi, F. Abild-Pedersen and J. K. Nørskov, *Inorg. Chem.*, 2018, **57**, 7222–7238.
30 K. S. Exner and H. Over, *Acc. Chem. Res.*, 2017, **50**, 1240–1247.
31 Z. W. Seh, J. Kibsgaard, C. F. Dickens, I. Chorkendorff, J. K. Nørskov and T. F. Jaramillo, *Science*, 2017, **355**, eaad4998.
32 Y.-H. Fang and Z.-P. Liu, *J. Am. Chem. Soc.*, 2010, **132**, 18214–18222.
33 C. F. Dickens, C. Kirk and J. K. Nørskov, *J. Phys. Chem. C*, 2019, **123**, 18960–18977.
34 J. T. Mefford, A. R. Akbashev, L. Zhang and W. C. Chueh, *J. Phys. Chem. C*, 2019, **123**, 18783–18794.
35 M. Bajdich, M. García-Mota, A. Vojvodic, J. K. Nørskov and A. T. Bell, *J. Am. Chem. Soc.*, 2013, **135**, 13521–13530.
36 Z. Lu, G. Chen, Y. Li, H. Wang, J. Xie, L. Liao, C. Liu, Y. Liu, T. Wu, Y. Li, A. C. Luntz, M. Bajdich and Y. Cui, *J. Am. Chem. Soc.*, 2017, **139**, 6270–6276.
37 J. Fester, M. García-Melchor, A. S. Walton, M. Bajdich, Z. Li, L. Lammich, A. Vojvodic and J. V. Lauritsen, *Nat. Commun.*, 2017, **8**, 14169.
38 Z. Zhao, P. S. Lamoureux, A. Kulkarni and M. Bajdich, *ChemCatChem*, 2019, **11**, 3423–3431.
39 M. Pourbaix, *Atlas of electrochemical equilibria in aqueous solutions*, National Association of Corrosion Engineers, Houston, TX, 2nd English edn, 1974.
40 H. Göhr, *Electrochim. Acta*, 1966, **11**, 827–834.
41 A. J. Bard, R. Parsons and J. Jordan, International Union of Pure and Applied Chemistry, *Standard Potentials in Aqueous Solutions*, Taylor & Francis Group, 1985.
42 J. B. Gerken, J. G. McAlpin, J. Y. C. Chen, M. L. Rigsby, W. H. Casey, R. D. Britt and S. S. Stahl, *J. Am. Chem. Soc.*, 2011, **133**, 14431–14442.
43 J. M. Tarascon, G. Vaughan, Y. Chabre, L. Seguin, M. Anne, P. Strobel and G. Amatucci, *J. Solid State Chem.*, 1999, **147**, 410–420.
44 Y.-C. Liu, J. A. Koza and J. A. Switzer, *Electrochim. Acta*, 2014, **140**, 359–365.
45 J. Rossmeisl, Z.-W. Qu, H. Zhu, G.-J. Kroes and J. K. Nørskov, *J. Electroanal. Chem.*, 2007, **607**, 83–89.
46 M. García-Mota, M. Bajdich, V. Viswanathan, A. Vojvodic, A. T. Bell and J. K. Nørskov, *J. Phys. Chem. C*, 2012, **116**, 21077–21082.

47 M. Zhang, M. de Respinis and H. Frei, *Nat. Chem.*, 2014, **6**, 362–367.
48 J. B. Goodenough and B. L. Cushing, *Handbook of Fuel Cells - Fundamentals, Technology and Applications*, Wiley, 2003, vol. 2, pp. 520–533.
49 E. D. German and A. M. Kuznetsov, *J. Phys. Chem.*, 1994, **98**, 6120–6127.
50 J. M. Saveant, *J. Am. Chem. Soc.*, 1987, **109**, 6788–6795.
51 R. R. Nazmutdinov, D. V. Glukhov, G. A. Tsirlina and O. A. Petrii, *Russ. J. Electrochem.*, 2002, **38**, 720–731.
52 K.-Y. Yeh and M. J. Janik, *J. Comput. Chem.*, 2011, **32**, 3399–3408.
53 J. A. Gauthier, C. F. Dickens, L. D. Chen, A. D. Doyle and J. K. Nørskov, *J. Phys. Chem. C*, 2017, **121**, 11455–11463.
54 A. Bergmann, D. Teschner, E. Martinez-Moreno, H. Dau, J. F. de Araújo, M. Gliech, P. Strasser, P. Chernev and T. Reier, *Nat. Commun.*, 2015, **6**, 8625.
55 A. Bergmann, T. E. Jones, E. M. Moreno, D. Teschner, P. Chernev, M. Gliech, T. Reier, H. Dau and P. Strasser, *Nat. Catal.*, 2018, **1**, 711–719.
56 M. W. Kanan, J. Yano, Y. Surendranath, M. Dincă, V. K. Yachandra and D. G. Nocera, *J. Am. Chem. Soc.*, 2010, **132**, 13692–13701.
57 M. Risch, A. Grimaud, K. J. May, K. a. Stoerzinger, T. J. Chen, A. N. Mansour and Y. Shao-Horn, *J. Phys. Chem. C*, 2013, **117**, 8628–8635.
58 X. Zhang, Y.-S. Chen, P. V. Kamat and S. Ptasinska, *J. Phys. Chem. C*, 2018, **122**, 13894–13901.
59 J. Suntivich, K. J. May, H. A. Gasteiger, J. B. Goodenough and Y. Shao-Horn, *Science*, 2011, **334**, 1383–1385.
60 S. Trasatti, *J. Electroanal. Chem. Interfacial Electrochem.*, 1980, **111**, 125–131.
61 J. T. Mefford, X. Rong, A. M. Abakumov, W. G. Hardin, S. Dai, A. M. Kolpak, K. P. Johnston and K. J. Stevenson, *Nat. Commun.*, 2016, **7**, 11053.
62 G. Mattioli, P. Giannozzi, A. Amore Bonapasta and L. Guidoni, *J. Am. Chem. Soc.*, 2013, **135**, 15353–15363.
63 F. Creazzo, D. R. Galimberti, S. Pezzotti and M.-P. Gaigeot, *J. Chem. Phys.*, 2018, **150**, 041721.
64 Y. Ping, R. J. Nielsen and W. A. Goddard, *J. Am. Chem. Soc.*, 2017, **139**, 149–155.
65 R. G. Delaplane, J. A. Ibers, J. R. Ferraro and J. J. Rush, *J. Chem. Phys.*, 1969, **50**, 1920–1927.
66 F. Pertlik, *Monatsh. Chem.*, 1999, **130**, 1083–1088.
67 L. Wang, T. Maxisch and G. Ceder, *Phys. Rev. B: Condens. Matter Mater. Phys.*, 2006, **73**, 195107.
68 A. Jain, G. Hautier, S. P. Ong, C. J. Moore, C. C. Fischer, K. A. Persson and G. Ceder, *Phys. Rev. B: Condens. Matter Mater. Phys.*, 2011, **84**, 045115.
69 K. A. Persson, B. Waldwick, P. Lazic and G. Ceder, *Phys. Rev. B: Condens. Matter Mater. Phys.*, 2012, **85**, 235438.
70 K. T. Winther, M. J. Hoffmann, J. R. Boes, O. Mamun, M. Bajdich and T. Bligaard, *Sci. Data*, 2019, **6**, 1–10.
71 Catalysis-Hub.org, https://www.catalysis-hub.org/publications/MeffordInterpreting2019, (accessed 21 August 2019).

